


PAPER • OPEN ACCESS

## Particle image velocimetry measurements in the vaneless space of a model Francis turbine under steady state operation

To cite this article: K F Sagmo *et al* 2021 *IOP Conf. Ser.: Earth Environ. Sci.* **774** 012026

View the [article online](#) for updates and enhancements.




**The Electrochemical Society**  
Advancing solid state & electrochemical science & technology

The ECS is seeking candidates to serve as the  
**Founding Editor-in-Chief (EIC) of ECS Sensors Plus,**  
a journal in the process of being launched in 2021

The goal of ECS Sensors Plus, as a one-stop shop journal for sensors, is to advance the fundamental science and understanding of sensors and detection technologies for efficient monitoring and control of industrial processes and the environment, and improving quality of life and human health.

*Nomination submission begins: May 18, 2021*



Nominate now!

# Particle image velocimetry measurements in the vaneless space of a model Francis turbine under steady state operation

K F Sagmo<sup>1</sup>, A Mærliè , P T Storli<sup>1</sup>

<sup>1</sup> Waterpower Laboratory, Norwegian University of Science and Technology, Alfred Getz Vei 4, 7491 Trondheim, Norway

E-mail: kristian.sagmo@ntnu.no

**Abstract.** Two-dimensional, two component particle image velocimetry (PIV) measurements of the guide-vane wake and vaneless space for a high head Francis model turbine are presented. Measurements have been carried out with a fixed head and rotational speed for a set of guide-vane openings representative of part load, high load and best efficiency operating points. The measured trajectory and strength of the guide vane wake for the different operating points is discussed in conjunction with the periodic velocity oscillations. It is hoped that the present measurements will aid in further analysis as well as provide an additional set of data for validation of numerical analyses.

*Keywords:* PIV, RSI, Vaneless space, Francis Turbine, Wake, Vortex Shedding

## 1. Introduction

Intermittent renewable energy sources, such as solar and wind power, has become increasingly widespread in recent years due to their promising potential of mitigating climate change by replacing fossil fuels [1]. This increase in intermittent energy sources into the global electrical power grid has raised questions related to grid stability, energy supply and demand, and so called integration costs[2, 3]. Unlike solar and wind power, hydropower is not strictly dependent on the weather conditions and offers more continuous power delivery while maintaining high energy conversion rates [4]. In response to the increase of intermittent energy sources in the power grid, hydraulic turbines such as the Francis turbine, are expected to be operated at off-design conditions more frequently [5]. This causes the need for a thorough understanding of the fluid flow inside a Francis turbine at different operating conditions.

Several of the undesirable phenomena in medium to high load Francis turbines have been linked to the rotor stator interaction (RSI)[5, 6, 7] and in general terms the flow in the vaneless space can be said to mediate this interaction[8]. While many numerical studies of the velocity field in the vaneless space of Francis turbines have been published (e.g.[9, 10]), fewer public experimental studies are known to the authors. One recent study that included both numerical and experimental investigations of the flow in the vaneless space of a low specific speed pump turbine was conducted by Hasamatuchi[11].



The turbine test rig at the Waterpower Laboratory at NTNU has been modified for optical access to allow for particle image velocimetry (PIV) measurements in the vaneless space. The Francis-99 turbine, on which the measurements have been carried out, has been part of the both the Francis-99 and HiFrancis workshop series and the turbine geometry is open to the public[12]. Together with previously published measurement data of the turbine efficiency hill chart[13], pressure pulsation amplitudes[14] and draft tube flow velocities[15, 16], the current measurements may serve as a complementary data set for comparison against numerical analyses of the same turbine.

## 2. Experimental setup and methods

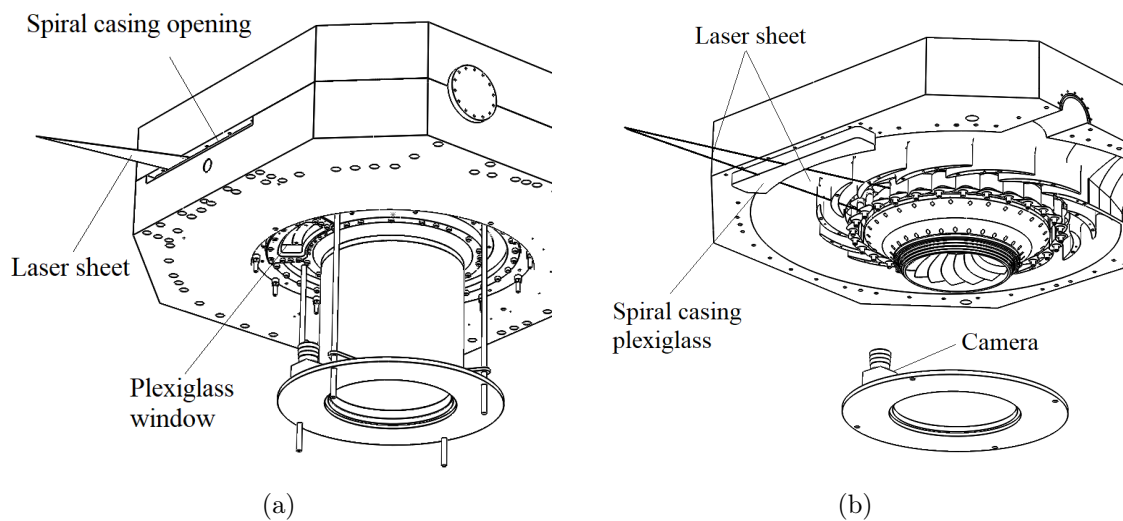


**Figure 1.** (a); Overview of the experimental setup. (b); View of setup with lower half of spiral casing removed.

The overall experimental setup is illustrated in figure 1. A Photron MiniUX 100 digital CMOS high speed camera was used for image capture, while a dual cavity Litron LDY 301 PIV laser was used for illumination. Optical access was granted by a set of plexi-glass windows, as well as plexi-glass stay-vanes and guide-vanes. The two-dimensional (2D), two component velocity field in the vane-less space was obtained by positioning the camera as illustrated with an orientation perpendicular to the laser sheets coming in from the side of the spiral casing.

### 2.1. Location of the measurement plane in the turbine

The position and reference frame orientation of the full resolution field of view (FOV) with respect to the turbine rotational axis are illustrated in figure 2(a)-(b). As can be seen, the region of interest was the wake of the guide-vane, leading into the runner. Although a group of guide-vanes adjacent to the measurement area were of plexi-glass material for optical access, the measured wake was of a standard, stainless steel guide-vane, with a trailing edge thickness,  $d$ , measured to about  $1.3 \pm 0.1$  mm. An enlarged camera image also indicating the full resolution FOV is illustrated in figure 3(a), while figure 3(b) shows a photo with the calibration plate installed. The images further serve to show the leading and trailing edges of the plexi-glass guide-vanes working as diverging and convergent lenses, creating gaps in the illuminating laser plane outside the FOV. Without optical index matching, this inherently limited the options of suitable FOV positions, but the current setup was deemed sufficient for the purpose of the measurements. Note

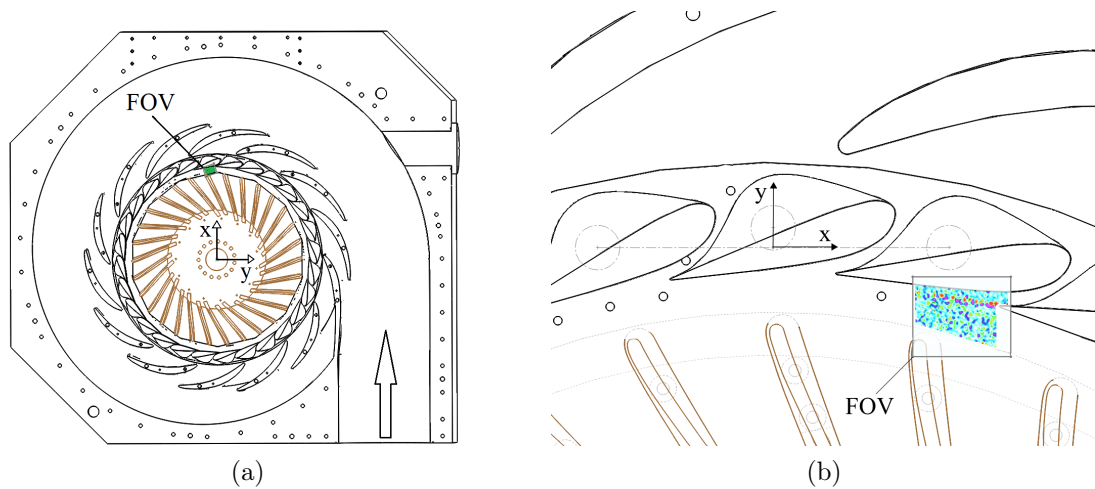


**Figure 2.** Location of field of view (FOV) with respect to the global turbine frame of reference, illustrated in view (a). In view (b); closer view of the FOV and orientation of the local reference frame.

that the calibration grid does not cover the complete guide vane passage, and consequently the uncovered parts of the measured vector fields later presented are deemed uncertain.

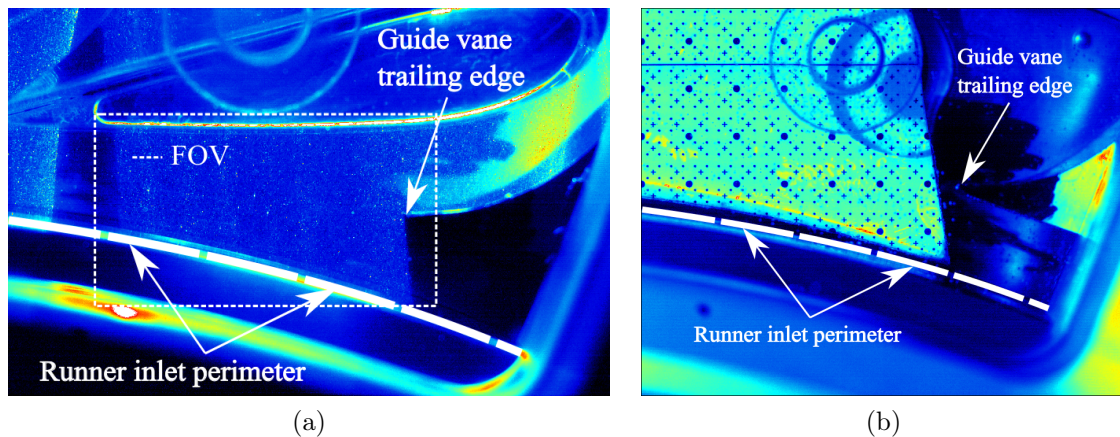


**Figure 3.** (a): An enlarged image indicating the approximate full resolution 1280 px x 1024 px field of view (FOV) utilised for the experiment by small white dashes. (b): Enlarged picture of the calibration plate positioning for overview.

## 2.2. Turbine operating parameters

All tests were conducted with the Francis-99 model turbine operating in steady state, for an average head of  $11.97 \pm 0.036$  mWc with the runner rotating at  $333.1 \pm 0.52$  rpm across all operating points. Measurements included guide-vane openings of  $4^\circ$ ;  $6.7^\circ$  (part load, PL);  $10^\circ$  (best efficiency point, BEP);  $12.4^\circ$  and  $14^\circ$  (high load, HL). In order to test for statistical convergence and hysteresis, two sets of measurements were taken at each guide vane angle starting from PL going to HL (ramp-up), as well as going from HL to PL (ramp-down). This gave a total of 4 image sets per guide-vane angle of operation.

**Table 1.** Summary of PIV recording parameters.

Resolution	1280 x 1024 pixels	1280 x 600 pixels
FOV	43.8 mm x 35.1 mm	43.8 mm x 20.5 mm
Vector field capture rate	0.2 kHz	4.166 kHz
Duration per vector set	21.84 s	1.79 s
Experimental velocity range	(3 - 12.4) m/s	
Image processing mode	Multi-pass cross-correlation	
Initial IA	64 x 64 pixels with 50% overlap	
Final IA	24 x 24 pixels with 50% overlap	
Mean tracer particle diameter	15.5 $\mu\text{m}$	
Tracer particle density	1.1 g/cm <sup>3</sup>	

### 2.3. PIV recording parameters

A summary of the PIV recording parameters are given in table 1. All image acquisition and PIV evaluation was handled with LaVisions imaging software DaVis 8.4. The recorded images were in a flow field with an average velocity of around 9.8 m/s. In order to obtain a particle shift of 5-6 px between successive images for the optical setup and field of view later described, the time delay,  $dt$ , between two particle images were varied between 15-17  $\mu\text{m}$ . Each particle image pair was illuminated by separate light pulses from the dual cavity laser. Laser light sheet overlap was checked and found adequate by cross correlation of particle images in a nearly stationary fluid. The full resolution images at 1280 px x 1024 px used for the time-averaged velocity fields later presented lasted for 1.79 seconds. This corresponded to roughly 300 runner blade passing's, or about 10 runner rotations. The vector fields evaluated from the low resolution images at 1204 px x 600 px were used in the frequency analysis later presented, due to the higher acquisition rate. All measurements were taken at a horizontal plane lying at a z-position corresponding to a vertical span position in the guide-vane passage of approximately 28.3 mm  $\pm$  1 mm, measured from the lower guide vane passage wall. The thickness of the laser sheet itself was estimated to approximately 0.8 mm. The calibration of images were done with a 3<sup>rd</sup> order polynomial mapping function, and the RMS fitting value obtained was 0.29 px with an average image scale of 29.2 px/mm.

The closed water loop was homogeneously seeded with tracer particles prior to conducting the measurements and average particle count was about 10 for the largest IA and about 5 for the smallest IA. Post processing of the evaluated vector fields with the universal outlier detection median filter proposed by Westerweel [17] showed only a negligible number of spurious vectors to be contained in the final vector field when the normalized residual threshold value for discarding a vector was set to 2. A set of vector fields were inspected for each of the operating points and the average cross correlation value of each vector field was generally found to be above 0.85. For the cross correlation evaluation DaVis 8.4 uses a 3 point Gaussian fit to estimate particle displacement and the observed particle size estimated by visual inspection was about 2-4 px for the results later presented. As such, this method should give sub-pixel accuracy in the estimation of the particle displacement [18, 19], and hence vector evaluation, thus minimizing any peak-locking effect. As a check the probability density function of the velocity components was inspected and the degree of peak-locking was found to be acceptable.

Further an uncertainty estimation for the instantaneous velocity fields was checked according to the method due to Wienke [20]. Overall, for the results later presented, this gave a maximum uncertainty in the order of 10% while generally the uncertainty observed to be in the range of 4%-6% relative to the approximate average velocity in the vaneless space. Finally, in order to estimate the uncertainty in the time-averaged velocity field magnitude  $\langle |\bar{V}| \rangle$ , the following



relation was applied [18];

$$\langle |\tilde{V}| \rangle = \frac{\sigma_{|V|}}{\sqrt{N_{eff}}}. \quad (1)$$

Here,  $\sigma_{|V|}$  denotes the standard deviation in  $|V|$  evaluated across all samples  $N$  of a measurement series.  $N_{eff}$  denotes the effective number of independent samples of  $|V|$ , evaluated through computation of the auto-correlation of the time-series of the instantaneous velocity amplitudes. In the case of the samples being completely independent, the number  $N_{eff}$  approaches the number of total samples  $N$ .

#### 2.4. Frequency analysis and energy maps as a function of frequency range

In an effort to look at the dominant frequencies in the measured velocity fields, the power spectra for both the x- and -y velocity components have been investigated. The spectra were obtained through discrete fourier transforms of the velocity fields, after a subtraction of the average velocity field for each operating point. A hanning weight function was used for windowing the data. Further, the power spectra profiles presented are spectrum averages over a 3x3 vector area around the specified points. Finally, energy fraction ( $EF$ ), maps were plotted by evaluating the kinetic energy fraction on a per point basis;

$$EF = \frac{E_{f_1-f_2}}{E_{total}}, \quad (2)$$

where  $E_{f_1-f_2}$  denotes the sum of energy contained within the frequency range  $f_1$  to  $f_2$ , and  $E_{total}$  is the total energy contained in the complete spectrum at a given point.

### 3. Results and discussion

#### 3.1. Instantaneous velocity field and frequency analysis

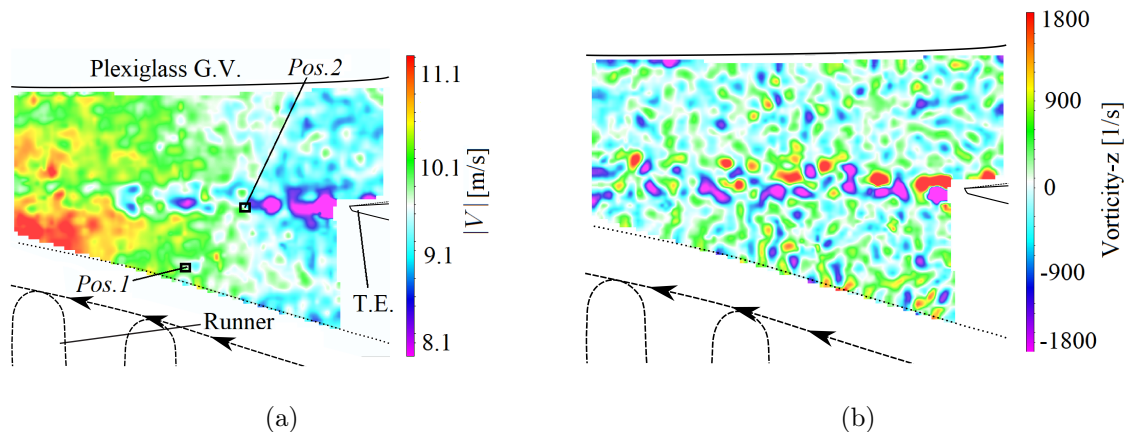


**Figure 4.** The resulting 2D velocity field from PIV measurements, colored according to (a); absolute velocity and (b); vorticity-z. *Pos.1* and *Pos.2* mark the approximate cross stream velocity sampling positions. T.E. denotes the guide-vane trailing edge position.

The instantaneous velocity field for best efficiency point operation is shown in figure 4(a). The wake of the guide vane is clearly visible, and the width of the velocity deficit zone near the trailing edge corresponds well with a trailing edge thickness of about 1.3 mm, though this is more clear in the time-averaged velocity profiles later presented. Figure 4(b) shows the vector field colored according to vorticity. Though clearly turbulent, a distinct vortex shedding street is visible, with alternating vortices extending several trailing edge diameters downstream.

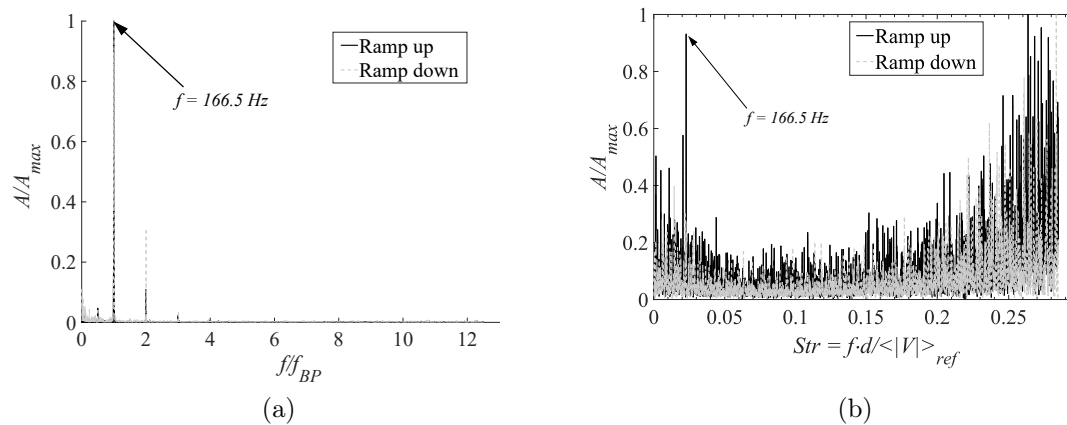


**Figure 5.** Amplitude spectra for different measurement samples obtained through FFT of the velocity component  $v$  along the y-axis, from the calculated velocity fields. The samples in (a) are spectra obtained from *Pos.1*, while the samples in (b) are obtained from *Pos.2*.

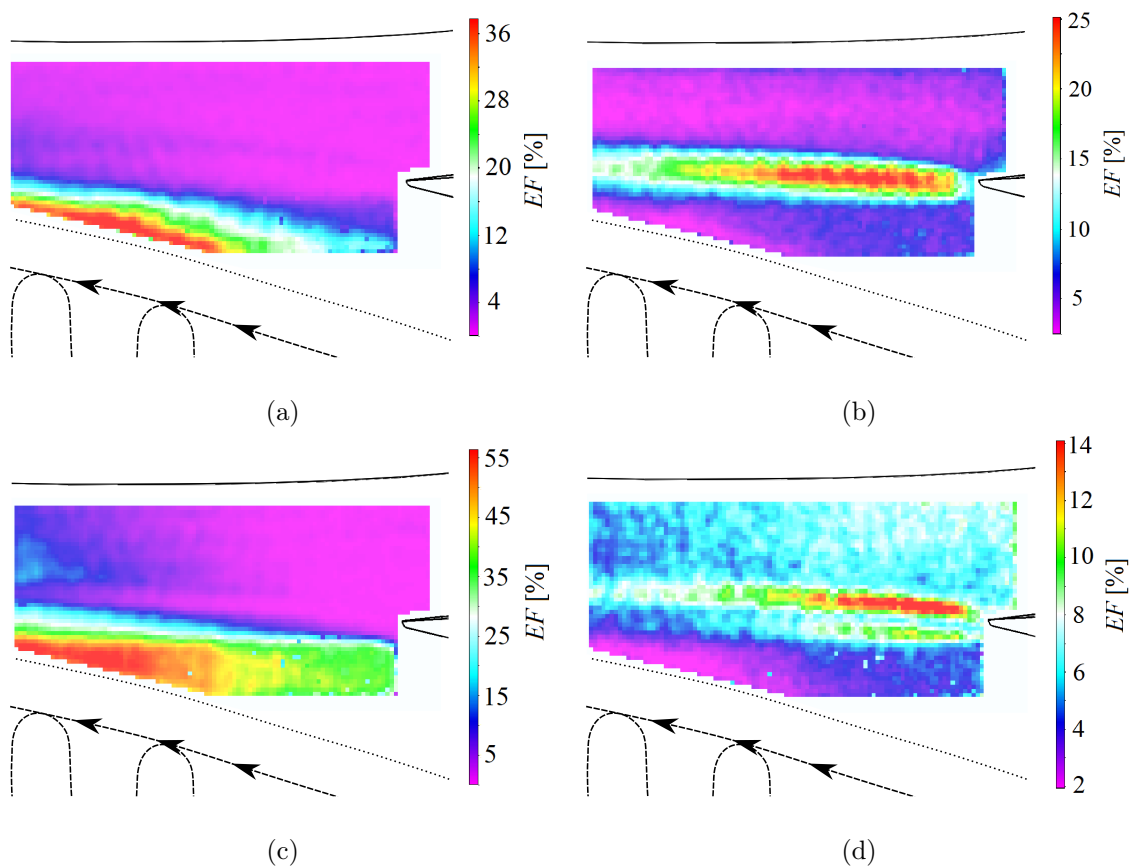


**Figure 6.** Energy fraction in frequency ranges corresponding to (a) 165-169 Hz and (b) 1870-2070 Hz for the velocity component along the y-axis, followed by corresponding fields for the velocity component along x-axis in (c) and (d).

Also indicated in figure 4(a) are two positions, *Pos.1* and *Pos.2*, from which the frequency spectra presented in figure 5 were obtained. The y-component, which is nearly perpendicular

to the mean flow direction for the given guide-vane angle, was sampled with a reduced field of view for an increased image rate of 4.166 kHz. While the runner blade passing frequency,  $f_{BP}$ , of 166.5 Hz is present in both spectra, the spectrum obtained at *Pos.1*, close to the runner, shows the peak most clearly. The spectrum obtained at *Pos.2*, plotted in figure 5(b), show what resembles a normal distribution of frequency peaks around a strouhal number of roughly 0.27 or a range of 1870-2070 Hz. Here the trailing edge thickness and the local average velocity in the vicinity of the trailing edge was used for scaling the strouhal number. The result is in good agreement with previous in-house measurements for shedding frequencies for a isolated hydrofoil in lock-off conditions[21], as well as measurements conducted by Heskestad and Olberts[22] for a similar trailing edge geometry. Further, one may argue that the broad range of peaks indicate no lock-in effect is present for the guide-vane investigated. In addition, the agreement between the two measurement sets indicate no marked hysteresis effects whether one is opening or closing the wicket gates.

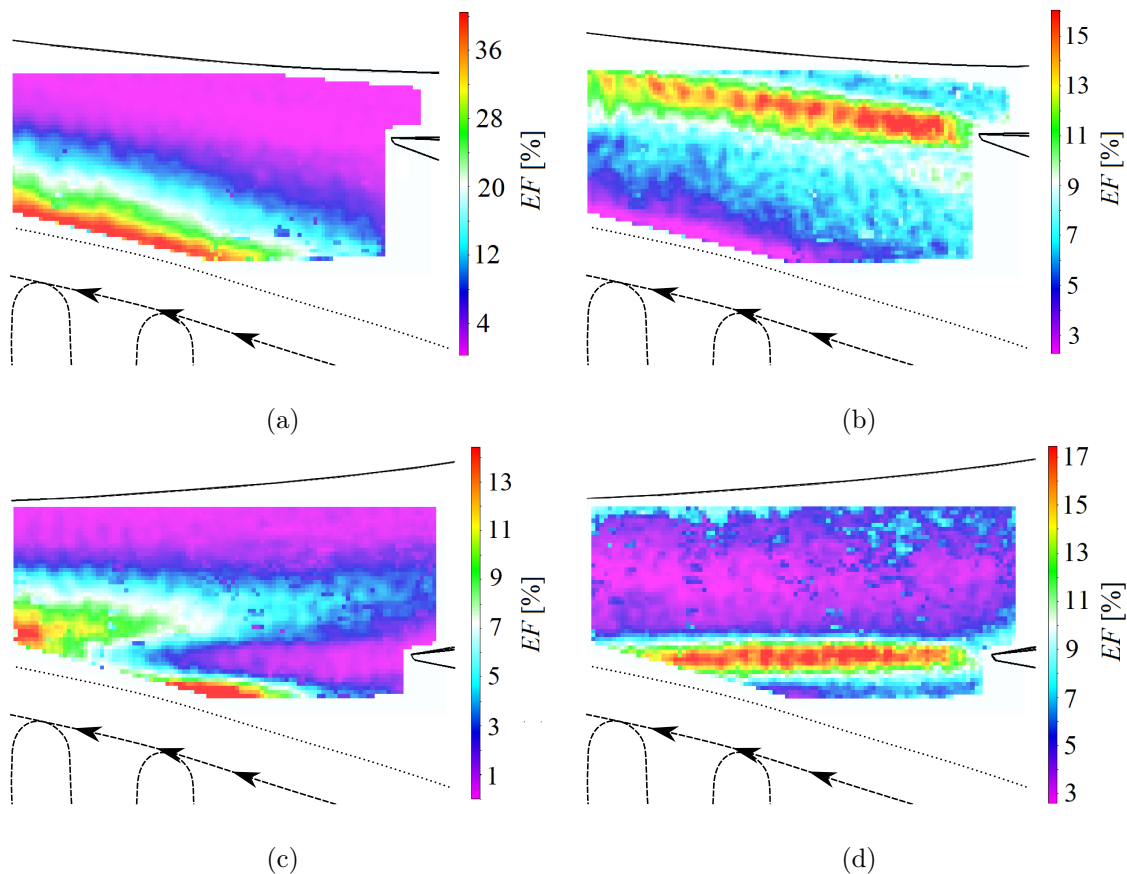


**Figure 7.** Energy fraction in frequency ranges corresponding to (a) 165-169 Hz, and (b) 1650-1850 Hz for velocity component along y-axis at PL operation. (c) and (d) give the corresponding fields for HL operation between frequency ranges of 165-169 Hz and 1844-2044 Hz, respectively.

Figure 6 shows field plots for the energy fraction contained within the fluctuating velocity components along the x- and y-axes at BEP, evaluated according to equation 2. The frequency ranges associated with the wake, figure 6(b) and (d), and runner blade passing characteristic frequencies, figure 6(a) and (c), were selected based upon the previously presented amplitude spectra. As is indicated by figure 6(c), a relatively large amount of the fluctuating energy in the x-velocity component is associated with the runner blade passing frequency. From the velocity



fields themselves it may seem that this energy content stems from a throttling effect occurring as the runner blade is passing close to the guide-vane. This periodic reduction in the cross section as seen by the fluid is enough to cause a significant pulsation in the velocity field, both radially and tangentially. While not explicit, this observation is inferred from the fluctuations along the x-and y-axis, which is oriented nearly tangentially and radially to the turbine's rotational frame of reference, respectively.

Analogously to figure 6, figure 7 show the same field plots for PL and HL operating points, though only for the velocity components along the y-axis. Figure 7(a) show the energy fraction associated with the runner blade passing frequency, while figure 7(b) show the energy fraction contained within the vortex shedding frequency range, both at PL operation. Figure 7(c) and (d) show the corresponding fields for HL operation. Note that, in order to extract the appropriate range of frequencies associated with the vortex shedding, the second sampling position indicated in figure 4 a) was moved to stay within the guide vane wake for these operating conditions. Interestingly, the effect of the runner blade passing is seen to be largely contained within the region circumferentially drawn by the the guide-vane wake. The exception is for HL operation, as shown in figure 7(c), where the interaction between the guide vane wake and the runner blade passing pulsations is more visible. Though not directly compared, this interaction implies that the kinetic energy contained within the wake of the guide vane, is similar in magnitude to the kinetic energy stemming from the apparent throttling effect, at least to some distance downstream of the guide vane trailing edge.

### 3.2. Time-averaged velocity fields

The following figures plot the time-averaged velocity fields for the range of guide-vane openings tested. An estimation of uncertainty in  $\langle |V| \rangle$ , as quantified by equation 1 gave a range of uncertainties everywhere less than 0.4 %, with the largest uncertainty associated with the trailing edge wake.

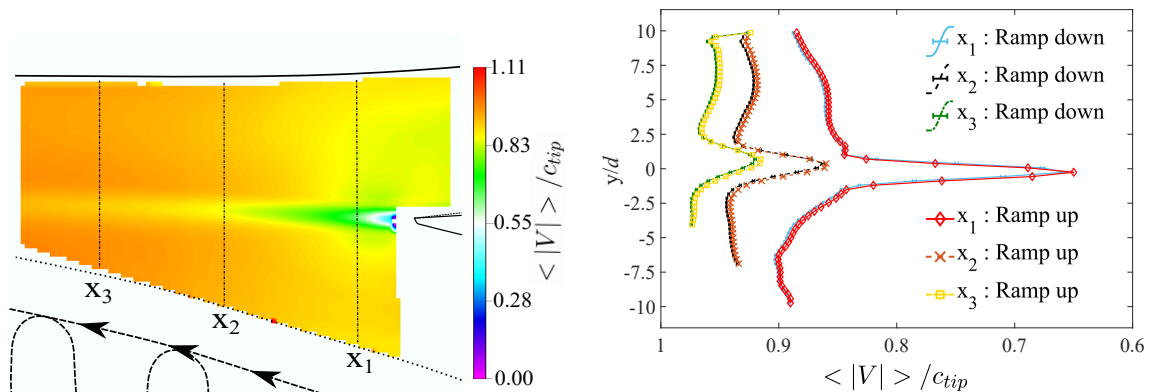


**Figure 8.** Time-averaged velocity measurements for a guide-vane opening of  $\alpha = 10^\circ$ . The three vertical lines at  $x_1 - x_3$  marked on the left hand side illustrates the location for the velocity profiles plotted on the right.

The time-averaged velocity field for BEP is given in figure 8. In order to take a closer look at the guide-vane wake recovery velocity magnitude profiles were extracted from the lines located at x-positions,  $x_1 - x_3$ , as shown. Here,  $x_1$  is located approximately  $3.6d$  downstream of the trailing edge tip, with  $x_2$  and  $x_3$  being successively shifted  $9.7d$  downstream. The results are plotted for measurements both at ramp up, and ramp down. Error-bars plotted for measurements during ramp-down represent the uncertainty estimate according to equation 1, but with the field average

value of the effective number of samples. The slight shift between the respective velocity profiles at ramp-up versus ramp-down measurements are readily explained by the uncertainty in the runner tip speed velocity,  $c_{tip}$ , used for normalization, as well as the uncertainty in the guide-vane opening angle. At  $x_3$ , corresponding to approximately  $23d$  downstream of the trailing edge tip, the wake is seen to be nearly recovered, with the maximum velocity deficit being around 5 %.

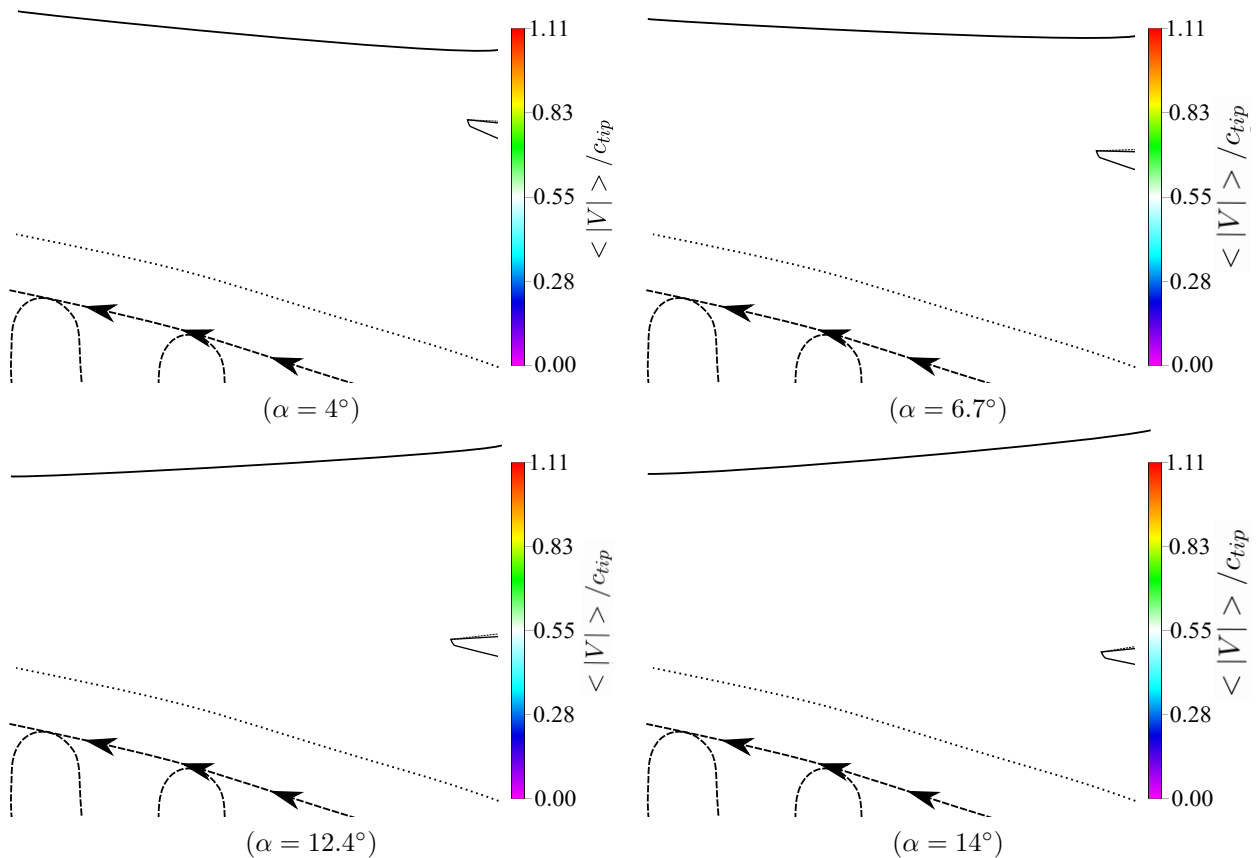


**Figure 9.** Time average velocity fields indicating wake trajectory for increasing guide vane angles.

Figure 9 show the remainder of the time-averaged velocity fields at increasing guide-vane openings. The guide-vane wake trajectory is generally observed to be closely aligned with the direction of the chord-line, as expected. Given the observed rate of recovery and trajectory for the different operating points, one may argue that the guide-vane wake will be largely recovered by the time it interacts with the runner leading edge, and so should induce only a small shift in the standing pressure field felt by the runner, for all operating points below a guide-vane opening angle of  $12.4^\circ$ . What the impact of the wake will be on the rotor-stator interaction effect is not clear however, since the complex interaction between vortices and inherent turbulence originating from the guide-vane could still play a part in for instance triggering boundary layer instabilities at the runner blades.

#### 4. Conclusion and future work

2D PIV measurements of the vaneless space flow field in the Francis-99 model turbine have been performed for a range of operating conditions. For the present model turbine, the average vector

fields obtained clearly indicate the trajectory of the guide-vane wakes and suggest that due to the rate of recovery, any shift in the standing pressure field felt by the runner due to the wakes should be small for all guide-vane opening angles below  $12.4^\circ$ . Even so, further quantification is needed for a proper conclusion.

A time-correlation for the PIV data with the runner blade position and pressure amplitudes in the channel would be interesting, to allow a more detailed investigation of the runner blade passing influence on the velocity field in the vane-less space. Further, transient measurements from very low guide vane angles up to PL, BEP and HL is suggested as part of future work.

### Acknowledgments

Einar Agnalt, Magne Tveit Bolstad and Steinar Gilberg Straume is gratefully acknowledged for their assistance during the first set of measurements and help in design of the experimental setup. Thanks to Igor Iliev for valuable feedback during the preparation of the document. Also, the help of the skilled technicians at the Waterpower laboratory is acknowledged. This study was made possible, in part, by funding from the HiFrancis research project and the Research Council of Norway.

### References

- [1] IPCC 2015 *Climate Change 2014: Mitigation of Climate Change: Working Group III Contribution to the IPCC Fifth Assessment Report: Energy Systems* (Cambridge University Press) pp 511–598
- [2] Acker T L, Robitaille A, Holttinen H, Piekutowski M and Tande J O G 2012 *Wind Engineering* **36** 1–17
- [3] Sorknæs P, Andersen A N, Tang J and Strøm S 2013 *Energy Strategy Reviews* **1** 174–180
- [4] Omar E, Abu-Rub H and Blaabjerg F 2014 *Renewable and Sustainable Energy Reviews* **39** 748–764
- [5] Goyal R and Gandhi B K 2018 *Renewable Energy* **116** 697 – 709 ISSN 0960-1481
- [6] Seidel U, Hübner B, Löfflad J and Faigle P 2012 *IOP Conference Series: Earth and Environmental Science* **15** 052010
- [7] Egusquiza E, Valero C, Huang X, Jou E, Guardo A and Rodriguez C 2012 *Engineering Failure Analysis* **23** 27–34
- [8] Zuo Z, Liu S, Sun Y and Wu Y 2015 *Renewable and Sustainable Energy Reviews* **41** 965 – 974 ISSN 1364-0321
- [9] Li Z, Wang Z, Wei X and Qin D 2016 *Journal of Fluids Engineering* **138** ISSN 0098-2202 061201
- [10] Trivedi C 2018 *Journal of Engineering for Gas Turbines and Power* **140** ISSN 0742-4795 112601
- [11] Hasmatuchi V 2012 *Hydrodynamics of a Pump-Turbine Operating at Off-Design Conditions in Generating Mode* Ph.D. thesis EPFL Lausanne Lausanne
- [12] Trivedi C, Gunnar Dahlhaug O, Selbo Storli P T and Kristian Nielsen T 2019 *Journal of Physics: Conference Series* **1296**
- [13] Trivedi C, Cervantes M J, Gandhi B K and Dahlhaug O G 2013 *Journal of Fluids Engineering* **135** ISSN 0098-2202 111102
- [14] Agnalt E, Solemslie B W and Dahlhaug O G 2019 *IOP Conference Series: Earth and Environmental Science* **240** 022040
- [15] Bergan C, Goyal R, Cervantes M J and Dahlhaug O G 2016 *IOP Conference Series: Earth and Environmental Science* **49** 062018
- [16] Sundstrom L R J, Amiri K, Bergan C, Cervantes M J and Dahlhaug O G 2014 *IOP Conference Series: Earth and Environmental Science* **22** 022012
- [17] Westerweel J and Scarano F 2005 *Experiments in Fluids* **39** 1096–1100 ISSN 1432-1114
- [18] LaVision GmbH 2017 Lavisoin software davis 8.4 product-manual, item-number: 1105xxx document name: 1003001 DaVis D84.pdf
- [19] Raffel M, Willert C E, Wereley S and Kompenhans J 2007 *Particle image velocimetry: a practical guide* 2nd ed (Heidelberg ; New York: Springer) ISBN 978-3-540-72307-3
- [20] Wienke B 2015 *Measurement Science And Technology* **26** 074002
- [21] Sagmo K F, Tengs E O, Bergan C W and Storli P T S 2019 *IOP Conf. Ser.: Earth Environ. Sci.* **240**
- [22] Heskestad G and Olberts D R 1960 *Journal of Engineering for Power* **82** 103–09